RSC Advances

PAPER

View Article Online
View Journal | View Issue

Cite this: *RSC Adv.*, 2025, **15**, 12629

Hollow flower-like WO_3@TiO_2 heterojunction microspheres for the photocatalytic degradation of rhodamine B and tetracycline†

Yinqi Yang,‡[a] Guoshuai Ma,‡[a] Xiaoli Hu,[a] Wei Wang, *[a] Zhonglin Du, [a] Yao Wang,[a] Xue-zhong Gong, [a] Haoyu Tan,[a] Fengxiang Guo*[b] and Jianguo Tang *[a]

In the context of sustainable development, the utilization of semiconductor materials for the degradation of dyes, antibiotics, heavy metals, and pesticides in wastewater under visible light has emerged as a focal point of contemporary research. In this investigation, a WO_3@TiO_2 composite was synthesized *via* a solvothermal method, with the composite exhibiting a molar ratio of 5% WO_3 to TiO_2 precursors demonstrating optimal photocatalytic degradation performance. This material achieved complete degradation of 20 mg per L Rhodamine B (RhB) dye and tetracycline (TC) antibiotic within 30 min. Furthermore, the effects of initial pollutant concentration and solution pH on catalytic efficacy were systematically explored. The findings revealed that at RhB concentrations below 40 mg L^{-1}, the degradation proceeded at an accelerated rate, with a rate constant exceeding 0.128 min^{-1}. The catalyst exhibited robust performance across a broad pH range, attaining peak degradation efficiency at pH ≈ 3. The exceptional photocatalytic prowess of the WO_3@TiO_2 composite is predominantly attributable to its distinctive hollow microstructure, the intimate interfacial synergy between WO_3 and TiO_2, and the efficient separation of photogenerated electrons and holes facilitated by the type-II heterojunction architecture.

Received 27th February 2025
Accepted 14th April 2025

DOI: 10.1039/d5ra01412c

rsc.li/rsc-advances

1. Introduction

The rapid pace of economic development and industrialization has precipitated a substantial discharge of industrial and domestic wastewater, markedly exacerbating water pollution and posing profound threats to human health and ecological systems.[1,2] Notably, the expansive production within the textile and apparel industries has positioned organic dyes as a predominant contributor to water contamination.[3] These dyes, characterized by aromatic ring structures and intricate heterogeneous biomass properties, exhibit carcinogenic, highly toxic, and non-biodegradable attributes.[4,5] To date, a plethora of techniques for treating dye-laden wastewater have been developed, encompassing physical adsorption,[6] membrane separation,[7] and advanced oxidation processes (AOPs),[8] among others. Within this spectrum, semiconductor photocatalysis has emerged as an environmentally benign and sustainable technology. Leveraging clean, renewable solar energy and employing semiconductor materials as catalysts, this approach facilitates the conversion and storage of solar energy through heterogeneous photocatalytic reactions, presenting an exemplary strategy to address both environmental pollution and energy scarcity.[9,10]

Presently, widely studied semiconductor photocatalysts include TiO_2,[11,12] ZnO,[13,14] WO_3,[15,16] and g-C_3N_4,[17,18] among others. Of these, TiO_2 stands out as one of the most extensively researched and broadly applied photocatalysts, owing to its superior catalytic performance, cost-effectiveness, and exceptional stability.[19–21] Nevertheless, the relatively wide bandgap of TiO_2 (approximately 3.2 eV) restricts its response to ultraviolet light (λ < 387 nm), which constitutes merely about 5% of the solar spectrum, thereby limiting its solar energy utilization efficiency. To broaden the photo-response range of TiO_2 and enhance its photocatalytic efficiency and solar energy harnessing capacity, researchers have proposed an array of optimization strategies, including elemental doping,[22] heterostructure engineering,[23,24] and morphological tailoring.[25,26]

The construction of heterojunction architectures represents a widely adopted strategy to enhance the separation efficiency of electron–hole pairs and suppress carrier recombination within photocatalysts.[27,28] Depending on the alignment of energy bands, heterojunctions are primarily classified into three categories: type-I, type-II, and type-III.[29] In a type-I heterojunction, the valence band maximum (VBM) of semiconductor B is positioned above that of semiconductor A, while its conduction

[a]*Institute of Hybrid Materials, National Center of International Research for Hybrid Materials Technology, National Base of International Science & Technology Cooperation, College of Materials Science and Engineering, Qingdao University, Qingdao 266071, P. R. China. E-mail: wangwei040901@163.com; tang@qdu.edu.cn*

[b]*Laoshan Laboratory, Qingdao 250316, China. E-mail: guofx123-4@163.com*

† Electronic supplementary information (ESI) available. See DOI: https://doi.org/10.1039/d5ra01412c

‡ Equal contribution.

band minimum (CBM) lies below that of semiconductor A. Consequently, under illumination, both the photogenerated electrons and holes in semiconductor A migrate toward and accumulate in semiconductor B, resulting in the inability to achieve effective carrier separation. In a type-III heterojunction, the conduction band of semiconductor B lies even below the valence band of A, rendering the transfer of electrons and holes to B unfeasible and similarly impeding separation.[30] In contrast, the type-II heterojunction features a staggered band alignment between semiconductors A and B, enabling spatial separation of photogenerated charge carriers and thereby markedly enhancing photocatalytic efficiency.[31,32] For instance, Kuang *et al.*[33] synthesized a TiO_2/UiO-66-NH_2 (TUN) type-II heterojunction photocatalyst *via* a solvothermal method coupled with *in situ* growth techniques. This configuration not only facilitates charge separation but also sustains elevated concentrations of Ti^{3+} through electron transfer, overcoming the inherent instability of Ti^{3+}. Consequently, the hydrogen production rate of TUN reached 593.53 μmol g^{-1} h^{-1}, a value 3.2 times higher than that of pristine TiO_2.

Furthermore, the morphology, size, and dispersion state of catalysts exert a profound influence on their photocatalytic degradation performance. Consequently, by judiciously modulating synthesis conditions, it is possible to refine catalyst morphology, yielding materials with expansive specific surface areas and abundant active sites.[34] For example, Shi *et al.*[35] synthesized a Bi_2O_3-sensitized TiO_2 hollow photocatalyst for the degradation of tetracycline under visible light. This TiO_2/Bi_2O_3 heterostructure exhibited enhanced visible-light absorption and exceptional cycling stability, attributable to the synergistic benefits of p–n junction interface engineering and the hollow architecture. The latter facilitates multiple internal light reflections, thereby augmenting light harvesting and utilization efficiency. Similarly, Wang *et al.*[36] reported a TiO_2@g-C_3N_4 core–shell quantum heterojunction, fabricated by polymerizing quantum-sized g-C_3N_4 onto anatase TiO_2 nanosheets (exposing the {001} facet). Owing to the intimate interfacial contact between TiO_2 and g-C_3N_4, the TiO_2@g-C_3N_4 (TCN) composite demonstrated optimal activity in the photocatalytic degradation of tetracycline, with 100 mg of TCN achieving complete decomposition of 2 mg per L tetracycline within 2 min. These examples underscore the critical role of optimizing heterojunction interface structures in enhancing photocatalytic performance, offering novel insights for the design of efficient solar-driven photocatalytic systems and advanced interface engineering strategies.

Building upon the aforementioned research context, this study aims to fabricate hollow flower-like WO_3 microspheres through a facile room-temperature synthesis method, followed by the deposition of dispersed TiO_2 nanosheets onto the etched WO_3 outer surface, thereby constructing a photocatalyst endowed with a high specific surface area and abundant active sites. Employing tetracycline and Rhodamine B (RhB) as target organic pollutants, the photocatalytic degradation performance of this catalyst was systematically assessed. Furthermore, by modulating the WO_3-to-TiO_2 ratio, the optimal heterojunction composition was elucidated. Additionally, the influence of pollutant concentration and solution pH on catalytic efficacy was meticulously investigated. These findings furnish both a theoretical framework and experimental foundation for the development of high-performance photocatalysts.

2. Experimental

2.1. Chemical reagents

Anhydrous ethanol (EtOH) was procured from Tianjin Fuyu Fine Chemical Co., Ltd. Sodium tungstate (Na_2WO_4) and calcium chloride ($CaCl_2$) were obtained from Shanghai Aladdin Biochemical Technology Co., Ltd. Oleic acid ($C_{18}H_{34}O_2$), tetrabutyl titanate (TBT), nitric acid (HNO_3), and hydrochloric acid (HCl) were sourced from Shanghai Macklin Biochemical Co., Ltd. Sodium hydroxide (NaOH), isopropanol (IPA), disodium ethylenediaminetetraacetate (EDTA-2Na), and *p*-benzoquinone (BQ) were supplied by Sinopharm Chemical Reagent Co., Ltd. All reagents employed were of analytical grade and utilized without further purification. Deionized water was used throughout the experimental procedures.

2.2. Catalyst preparation

The synthesis of flower-like hollow WO_3 microspheres proceeded as follows: initially, 1.1 g of $CaCl_2$ was dissolved in 50 mL of deionized water under magnetic stirring until a fully transparent solution (solution A) was obtained. Concurrently, 1.98 g of $Na_2WO_4 \cdot 2H_2O$ was dissolved in 50 mL of deionized water with stirring until complete dissolution, yielding solution B. Under vigorous agitation, solution B was slowly added dropwise to solution A, during which the mixture transitioned from colorless and transparent to a white $CaWO_4$ suspension. After stirring for 2 h, the precipitate was separated by centrifugation, washed twice sequentially with deionized water and anhydrous ethanol, and the resulting $CaWO_4$ precipitate was dried in a vacuum oven at 60 °C for 12 h. The dried white sample was ground uniformly, and 0.5 g of this powder was mixed with 10 mL of concentrated HNO_3 (65 wt%) and stirred for 5 h. The resulting light green WO_3 precipitate was isolated by centrifugation and washed with deionized water until neutral. To enhance the crystallinity of WO_3 and eliminate volatile impurities, the dried and ground product was calcined in a muffle furnace, with the temperature ramped at a rate of 1.5 °C min^{-1} to 350 °C and maintained for 3 h, ultimately yielding flower-like hollow WO_3 microspheres.

The WO_3@TiO_2 heterojunction was synthesized *via* a solvothermal method as follows: a predetermined quantity of WO_3 powder was dispersed in 20 mL of oleic acid solution, followed by the addition of 1 mL of concentrated hydrochloric acid (37 wt%). The mixture was magnetically stirred for 30 min and then subjected to ultrasonication for an additional 30 min to ensure uniform dispersion. Subsequently, 1 mL of tetrabutyl titanate (TBT) was slowly added dropwise, and stirring was continued for 4 h to facilitate thorough reaction. The resulting mixture was transferred to a 50 mL Teflon-lined autoclave and heated at 190 °C for 3 h. After the reaction system naturally cooled to room temperature, the product was collected by

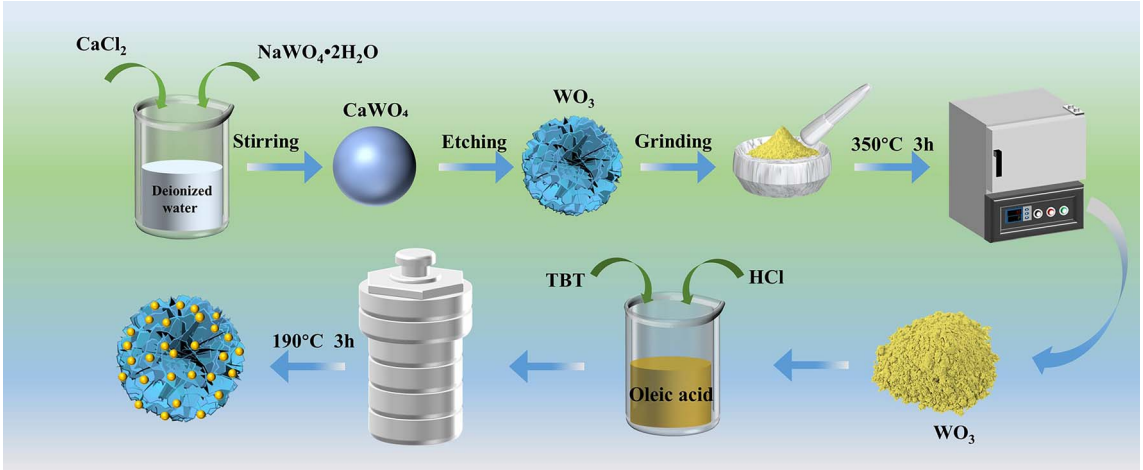

Fig. 1 Schematic illustration of the synthesis process of WO_3@TiO_2 heterojunction composite material.

centrifugation and washed three times sequentially with deionized water and anhydrous ethanol to remove residual organic matter. The obtained precipitate was dried in a vacuum oven at 65 °C for 12 h and ground uniformly to yield the WO_3@TiO_2 heterojunction material. By adjusting the molar ratio (%) of WO_3 to TBT, a series of WO_3@TiO_2 samples with varying WO_3 contents were prepared and designated as *x*% WT. As a control, a pure TiO_2 sample was synthesized under identical conditions without the addition of WO_3. Fig. 1 provides a schematic illustration of the preparation procedure employed in this study.

2.3. Characterization

The crystalline structure of the samples was analyzed using X-ray diffraction (XRD) on a powder X-ray diffractometer (Ultima XV) with Cu-Kα radiation, a scanning speed of 2° min^{-1}, and a 2θ range of 10–80°, operating at 36 kV and 30 mA. The surface morphology was examined *via* scanning electron microscopy (SEM, JSM-6390LV) in conjunction with energy-dispersive X-ray spectroscopy (EDS) to determine the elemental distribution. Transmission electron microscopy (TEM, JEM-1200EX, accelerating voltage: 100 kV) was employed to further investigate the microstructural characteristics of the samples. X-ray photoelectron spectroscopy (XPS) measurements were performed using a Thermo Scientific Escalab 250 spectrometer with an Al-Kα source. The UV-Vis diffuse reflectance spectra (UV-Vis DRS) were recorded on a PerkinElmer Lambda 750S spectrophotometer to analyze the optical absorption properties and bandgap characteristics. Photoluminescence (PL) spectra were obtained using a Hitachi F-7000 fluorescence spectrometer under 350 nm excitation to evaluate the radiative recombination dynamics of photogenerated charge carriers.

The specific surface area was determined *via* the Brunauer–Emmett–Teller (BET) method through nitrogen adsorption–desorption experiments conducted on a Micromeritics TriStar II 3020 system, with samples pre-degassed under vacuum at 100 °C for 5 h. The electrochemical properties were assessed using a CHI660E electrochemical workstation in a three-electrode system, with a 0.1 M Na_2SO_4 solution as the electrolyte, a platinum sheet as the counter electrode, and an Ag/AgCl electrode as the reference electrode. The working electrode was prepared by dispersing 10 mg of the sample in a mixture of 1 mL ethanol and 50 μL Nafion solution, followed by 10 min of ultrasonication to ensure uniform dispersion. The resulting suspension was drop-cast onto an indium tin oxide (ITO) glass substrate (4 × 1 cm^2, with a coating area of 2 × 1 cm^2) and vacuum-dried at 80 °C for 12 h. The transient photocurrent response and electrochemical impedance spectroscopy (EIS) measurements were conducted under constant potential conditions.

Electron spin resonance (ESR) spectroscopy (Bruker EMX PLUS) was utilized to detect superoxide radicals ($^{\bullet}O_2^-$) generated under illumination, using 5,5-dimethyl-1-pyrroline *N*-oxide (DMPO) as the spin-trapping agent. The mineralization efficiency was quantified by total organic carbon (TOC) analysis using a Shimadzu TOC-L analyzer equipped with a non-dispersive infrared detector.

2.4. Photocatalytic experiments

The photocatalytic activity was evaluated using an XPA-7 photochemical reaction system (Nanjing Xujing Electromechanical Factory), with Rhodamine B (RhB, 20 mg L^{-1}) and tetracycline (TC, 20 mg L^{-1}) as the target pollutants. The standard testing procedure was as follows: 20 mg of the photocatalyst was dispersed in 40 mL of pollutant solution and ultrasonicated for 1 min to ensure uniform dispersion. Prior to illumination, the suspension was magnetically stirred in the dark for 30 min to establish an adsorption–desorption equilibrium. A 350 W xenon lamp equipped with a 420 nm cutoff filter served as the visible-light source, and a circulating water bath was employed to maintain a constant reaction temperature of (25 ± 2) °C. During irradiation, 3 mL of the supernatant was withdrawn at predetermined time intervals. To prevent further photocatalytic reactions, the collected samples were immediately subjected to high-speed centrifugation to separate the catalyst particles, after which the precipitate was returned to the

reaction solution. The clarified supernatant was placed in a quartz cuvette, and the characteristic absorption peaks of RhB (554 nm) and TC (357 nm) were measured using a UV-Vis spectrophotometer. The pollutant concentration was determined based on the Lambert–Beer law.[37] Throughout the photodegradation process, the normalized concentration (C_t/C_0) was proportional to the normalized absorbance (A_t/A_0), where C_0 represents the initial pollutant concentration and C_t denotes the concentration at time t under irradiation. According to previous literature reports, when the initial dye concentration is not excessively high, the degradation kinetics of dyes typically follow a pseudo-first-order reaction model based on the Langmuir–Hinshelwood mechanism:[38]

$$\ln\left(\frac{C_t}{C_0}\right) = \ln\left(\frac{A_t}{A_0}\right) = kt \quad (1)$$

where k is the pseudo-first-order reaction rate constant.

The degradation efficiency (η) of the pollutant is calculated using the following equation:

$$\eta = \frac{A_0 - A_t}{A_0} \times 100\% \quad (2)$$

In the radical scavenging experiments, isopropanol (IPA) was employed as a scavenger for hydroxyl radicals ($^{\bullet}OH$), disodium ethylenediaminetetraacetate (EDTA-2Na) was used to quench holes (h^+), and *p*-benzoquinone (BQ) served as a scavenger for superoxide radicals ($^{\bullet}O_2^-$). The concentration of each scavenger was maintained at 2 mmol L^{-1}.

3. Results and discussion

3.1. Microstructural analysis

The morphology and structure of TiO_2, WO_3, and WO_3@TiO_2 composite materials were investigated using scanning electron microscopy (SEM) and transmission electron microscopy (TEM). The precursor $CaWO_4$, synthesized *via* the reaction between $CaCl_2$ and Na_2WO_4, exhibited smooth-surfaced, uniformly sized solid microspheres (Fig. S1†). Fig. 2(a)–(c) illustrate the microstructure of WO_3. The SEM images reveal that the solid $CaWO_4$ microspheres were transformed into hollow WO_3 microspheres through a combination of chemical reaction and etching effects induced by HNO_3. The surface of the resulting WO_3 microspheres was composed of self-

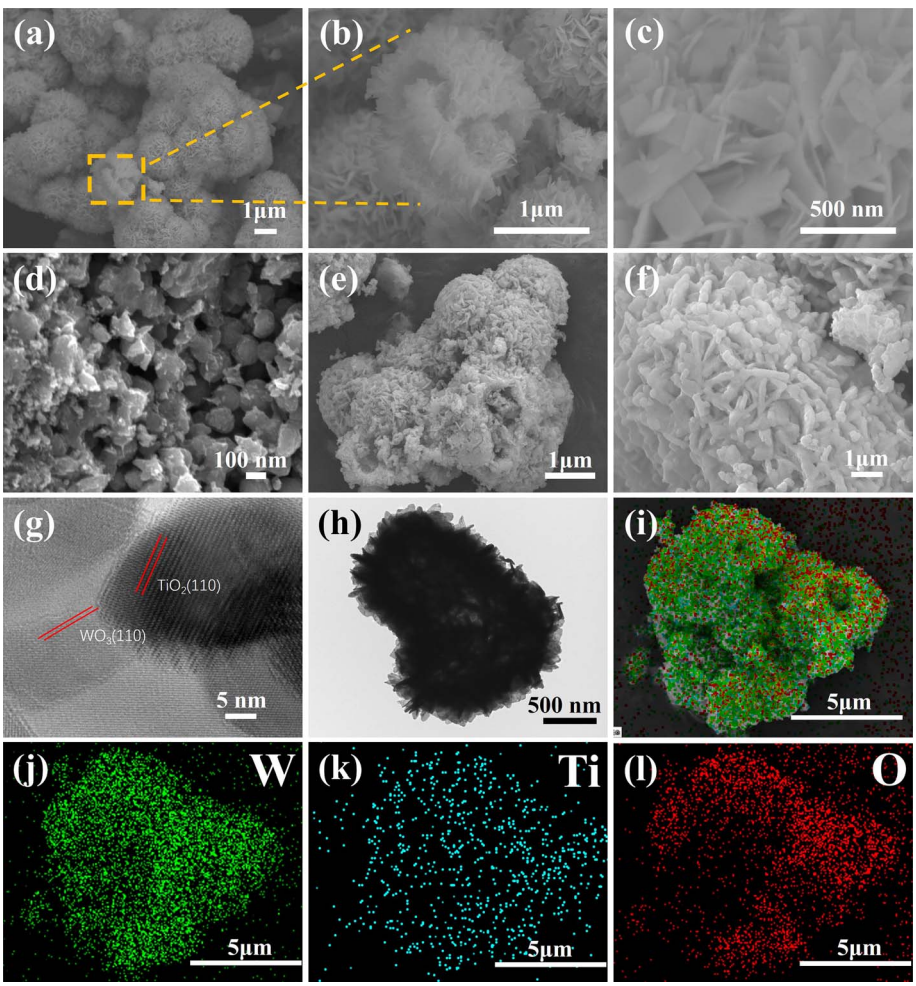

Fig. 2 (a and b) SEM images of WO_3; (c) high-magnification SEM image of WO_3; (d) SEM image of TiO_2; (e and f) SEM images of 5% WT; (g) SAED pattern of 5% WT; (h) TEM image of 5% WT; (i–l) EDS elemental distribution maps of 5% WT.

assembled nanosheets. This transformation was primarily attributed to the synergistic effect of the chemical reaction and etching process facilitated by HNO_3: HNO_3 reacted with $CaWO_4$ to generate WO_3 and soluble $Ca(NO_3)_2$, thereby dissolving Ca^{2+} and leaving behind a solid WO_3 framework. Simultaneously, HNO_3 selectively etched the WO_3 surface, promoting the formation of a nanosheet-assembled structure while partially dissolving the internal material to create a hollow cavity. Consequently, the initially smooth solid microspheres evolved into flower-like hollow structures composed of nanosheets, each with a diameter of approximately 300 nm. The unique hollow architecture and nanosheet-stacked configuration are advantageous for photocatalysis. The hollow structure facilitates multiple light scattering and reflection, extending the optical path and enhancing light absorption efficiency. Compared to solid microspheres, these hollow microspheres possess a significantly larger specific surface area, providing more active sites for photocatalytic reactions and improving pollutant adsorption and degradation efficiency. Additionally, the hollow architecture shortens the migration distance of photogenerated charge carriers to the surface, thereby reducing recombination rates within the bulk phase and enhancing overall photocatalytic performance.[39]

Fig. 2(d) shows that pure TiO_2 exhibits a disordered spherical morphology with a diameter of approximately 200 nm. In contrast, Fig. 2(e) and (f) reveal that in the WO_3@TiO_2 composite material, WO_3 nanosheets are uniformly covered with TiO_2 nanoparticles on their surface. Compared to the smooth and clean surface of pure WO_3 nanosheets, the composite material displays a significantly increased surface roughness and a noticeable increase in nanosheet thickness. Notably, the TiO_2 particles form a tightly intercalated interface with the WO_3 substrate. This unique morphological feature facilitates the interfacial transport and effective separation of photogenerated charge carriers, thereby suppressing the recombination of electron–hole pairs.[40,41] Fig. 2(g) displays a high-resolution TEM image of the 5% WT composite material, where clear lattice fringes with spacings of approximately 0.38 nm and 0.285 nm are observed, corresponding to the (110) plane of TiO_2 and the (110) plane of the flower-like WO_3 microspheres, respectively.[42] Fig. 2(h) further demonstrates the TEM image of the 5% WT catalyst, where WO_3 retains its nanosheet structure and hollow features, while TiO_2 is uniformly distributed on the surface of the WO_3 nanosheets. This observation is consistent with the SEM results. To further investigate the distribution of TiO_2 within the WO_3 flower-like structure, EDS mapping was performed to analyze the elemental distribution in the composite material. Fig. 2(i)–(l) indicate that the WO_3@TiO_2 catalyst primarily consists of Ti, W, and O elements, with Ti being evenly distributed across the catalyst surface. This confirms that TiO_2 nanoparticles are uniformly dispersed within the hollow WO_3 framework.

3.2. Crystalline structure

The crystal structures of TiO_2, WO_3, and WO_3@TiO_2 composites were characterized by X-ray diffraction (XRD). As shown in Fig. 3(a), pure TiO_2 exhibits characteristic diffraction peaks at 2θ = 25.32°, 37.87°, 48.04°, 53.92°, 55.12°, and 62.73°, corresponding to the (101), (004), (200), (105), (211), and (204) crystal planes of the anatase phase (JCPDS no. 21-1272).[43,44] The XRD pattern of pristine WO_3 displays distinct peaks at 13.9°, 23.4°, 24.3°, 27.9°, 33.9°, 36.9°, 49.8°, 55.9°, and 63.2°, which are well-indexed to the (001), (110), (200), (111), (201), (220), (221), and (401) planes of hexagonal-phase WO_3 (JCPDS no. 33-1387).[45] In the composite materials, the diffraction pattern is dominated by the characteristic peaks of anatase TiO_2, while the WO_3 peaks exhibit significantly weaker intensity. Notably, as the WO_3 content in WO_3@TiO_2 increases, two new distinct diffraction peaks emerge at 27.9° and 33.9°, assigned to the (201) and (220) planes of WO_3, respectively. However, most characteristic peaks of WO_3 remain barely detectable in the WO_3@TiO_2 samples, likely due to the relatively low WO_3 content within the heterojunction. Importantly, no additional diffraction peaks are observed in the composites, indicating that the introduction of TiO_2 does not alter the crystalline structure of WO_3.[46]

3.3. Specific surface area analysis

The specific surface areas of WO_3, TiO_2, and various WO_3@TiO_2 composites were determined by nitrogen adsorption–desorption measurements. As illustrated in Fig. 3(b), all samples exhibit characteristic type IV isotherms: at low relative

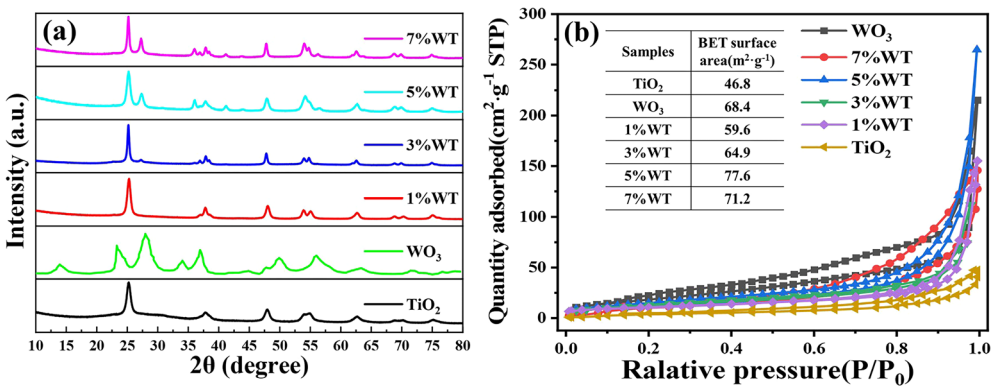

Fig. 3 (a) XRD spectra and (b) N_2 adsorption–desorption curves of pure TiO_2, WO_3 and different WO_3@TiO_2 samples.

pressures, the N_2 adsorption capacity remains limited, but it increases significantly with rising relative pressure, accompanied by a distinct hysteresis loop, confirming the mesoporous structure of the materials. The specific surface areas of pristine TiO_2 and WO_3 were measured at 46.8 $m^2\ g^{-1}$ and 68.4 $m^2\ g^{-1}$, respectively. Notably, the specific surface area of the WO_3@TiO_2 composites initially increases and then decreases with varying WO_3 content, reaching a maximum value (77.6 $m^2\ g^{-1}$) for the 5% WT sample before declining. The enhanced surface area in the composites is primarily attributed to the uniform deposition of TiO_2 nanoparticles on the WO_3 nanosheets, which increases surface roughness. This enlargement in surface area not only provides additional adsorption sites for pollutants but also exposes more catalytically active centers, thereby significantly improving photocatalytic performance.[40] At low WO_3 content, where TiO_2 dominates, excessive TiO_2 accumulation may block the surface pores of WO_3, resulting in a composite surface area intermediate between those of pure TiO_2 and WO_3. However, at 5% WO_3 loading, TiO_2 nanoparticles are likely uniformly dispersed on the WO_3 surface, introducing supplementary porosity and roughness without structural obstruction. This synergistic effect leads to a specific surface area exceeding that of pure WO_3. Beyond 5% WO_3 content, the surface area begins to decline, possibly due to insufficient TiO_2 nanoparticles for complete surface coverage, reducing the overall roughness of WO_3.

3.4. Surface chemical states

A systematic investigation of the surface elemental composition and chemical states of pure TiO_2, WO_3, and WO_3@TiO_2 composites was conducted using X-ray photoelectron spectroscopy (XPS). As shown in Fig. 4(a), the characteristic peaks of W, Ti, and O elements were detected in the WO_3@TiO_2 composite, corroborating the EDS results and confirming the successful loading of TiO_2 nanoparticles onto the WO_3 surface. The C signal observed in all samples primarily originated from environmental contamination and instrument artifacts. High-resolution Ti 2p spectra analysis (Fig. 4(e)) revealed that TiO_2 exhibits characteristic peaks at binding energies of 458.6 eV (Ti $2p_{3/2}$) and 464.2 eV (Ti $2p_{1/2}$), with a spin–orbit splitting energy of 5.6 eV, confirming the presence of Ti^{4+}.[47,48] Notably, compared to pure TiO_2, the Ti 2p peaks in the composite shifted toward higher binding energies by 0.2 eV and 0.3 eV, respectively. This chemical shift indicates strong interfacial interactions between TiO_2 and WO_3.[49] The deconvolution of O 1s spectra (Fig. 4(c) and (f)) demonstrated that both WO_3 and WO_3@TiO_2 exhibit two resolved peaks: a dominant peak at ~529 eV attributed to lattice oxygen in metal–oxygen bonds (M–O, M = Ti/W), and a shoulder peak at 530.3 eV associated with surface hydroxyl groups and adsorbed oxygen species.[50,51] High-resolution fitting of the W 4f spectra (Fig. 4(d)) showed that pristine WO_3 displays binding energies at 35.53 eV (W $4f_{7/2}$) and 37.72 eV (W $4f_{5/2}$), consistent with the W^{6+} oxidation state.[52,53] In contrast, the WO_3@TiO_2 composite (Fig. 4(g)) exhibited positive shifts of these peaks to 35.62 eV and 37.78 eV, respectively. The increased binding energies suggest that WO_3 acts as an electron acceptor in the heterojunction, further evidencing efficient electron interactions between TiO_2 and WO_3.[42,54]

3.5. Optical properties

The optical absorption characteristics and bandgap of the synthesized samples were analyzed using UV-Vis diffuse reflectance spectroscopy (UV-Vis DRS). As shown in Fig. 5(a), pure WO_3 exhibits a pronounced absorption edge around 500 nm, corresponding to its intrinsic narrow bandgap (approximately 2.6 eV). Pure TiO_2 primarily absorbs UV light in the range of 200–400 nm, with its absorption edge located around 400 nm, attributed to its inherent wide bandgap (approximately 3.2 eV). In contrast, as the WO_3 content increases, the absorption edge of the WO_3@TiO_2 composite

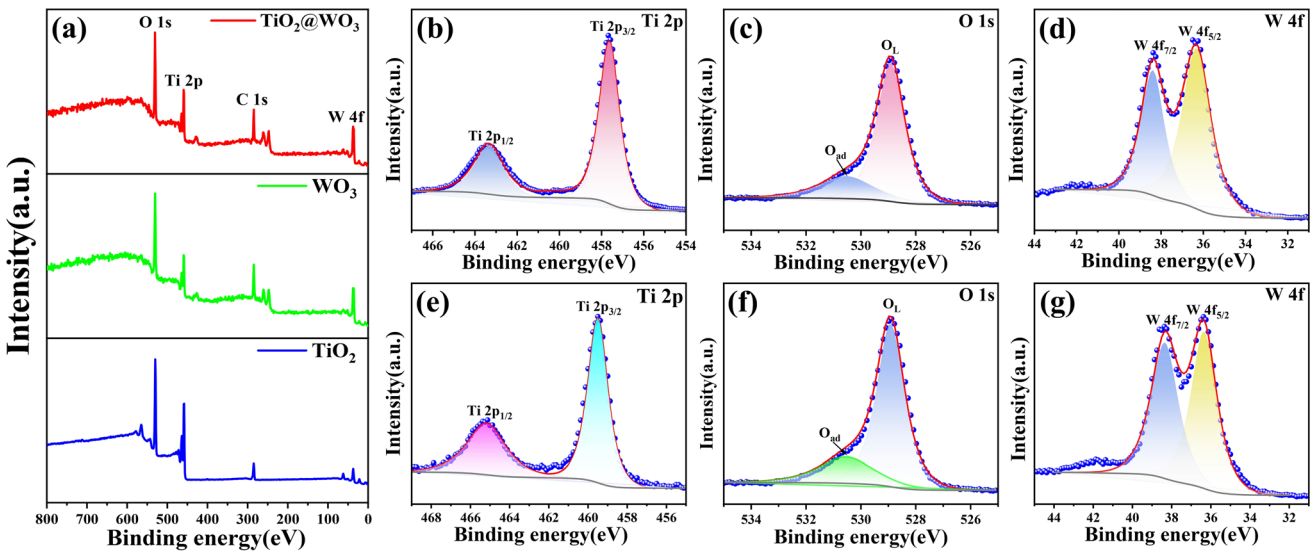

Fig. 4 (a) Full scan XPS spectra of TiO_2, WO_3, and WO_3@TiO_2; (b) Ti 2p XPS spectrum of TiO_2; (c) O 1s XPS spectrum of WO_3; (d) W 4f XPS spectrum of WO_3; (e) Ti 2p XPS spectrum of WO_3@TiO_2; (f) O 1s XPS spectrum of WO_3@TiO_2; (g) W 4f XPS spectrum of WO_3@TiO_2.

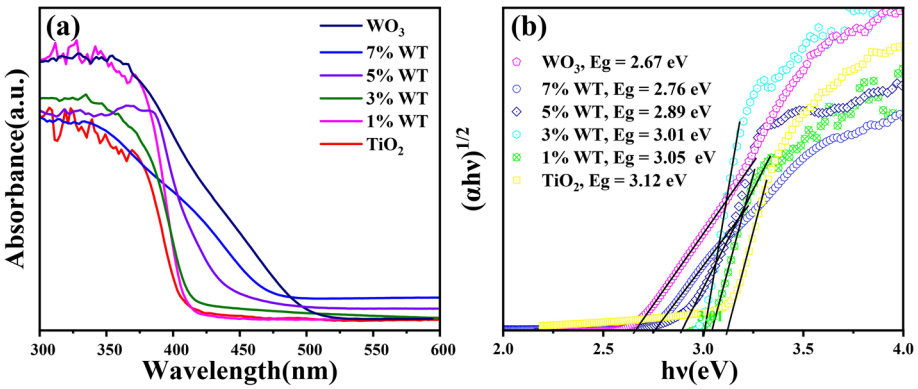

Fig. 5 (a) UV-visible diffuse reflectance spectra and (b) Tauc plots of pure TiO_2, WO_3, and different WO_3@TiO_2 samples.

material gradually shifts toward the visible light region, demonstrating enhanced optical absorption capability. This improved light absorption property facilitates the generation of more photogenerated charge carriers during the photocatalytic process, thereby enhancing the efficiency of photocatalytic degradation reactions.

The bandgaps of all materials were calculated using the Tauc formula:[55,56]

$$(\alpha h\nu)^n = K(h\nu - E_g) \quad (3)$$

where α is the absorption coefficient, h is Planck's constant, ν is the frequency, K is a constant, and E_g is the bandgap width of the semiconductor. For direct bandgap semiconductors, $n = 2$; for indirect bandgap semiconductors, $n = 1/2$. Anatase TiO_2 and WO_3 are both indirect bandgap semiconductors, so $n = 1/2$.[57,58] WO_3@TiO_2 composites are considered as indirect bandgap semiconductors, so $n = 1/2$. Plot with $h\nu$ as the abscissa and $(\alpha h\nu)^n$ as the ordinate, where $h\nu$ is calculated as 1240/wavelength. It should be noted that the ordinate of the UV-Vis diffuse reflectance spectrum is usually the absorbance value (Abs), which is proportional to α, so Abs can be used instead of α as the ordinate, that is, $(\text{Abs} \times h\nu)^n$. By extrapolating the intersection of the straight-line part of the graph and the horizontal axis, the band gap width of the semiconductor can be obtained. As shown in Fig. 5(b), the band gap widths of TiO_2, WO_3, 1% WT, 3% WT, 5% WT and 7% WT are 3.12, 2.67, 3.05, 3.01, 2.89 and 2.76 eV, respectively, which shows that loading TiO_2 on WO_3 nanoflowers can effectively reduce the energy gap of TiO_2.

The recombination dynamics of photogenerated charge carriers were investigated using steady-state/transient photoluminescence (PL) spectroscopy. When a semiconductor absorbs photons with energy exceeding its bandgap, electrons are excited from the valence band to the conduction band, generating electron–hole pairs. The subsequent radiative recombination of these charge carriers results in photon emission, with the PL intensity directly correlating with the recombination rate. Higher PL intensity indicates more rapid charge recombination and lower probability of carrier migration to catalyst surfaces, which is detrimental to photocatalytic activity.[59] All samples exhibited broad visible emission bands in the 420–470 nm range (corresponding to photon energies of 2.5–2.9 eV). As shown in Fig. 6(a), a systematic decrease in PL intensity was observed with increasing WO_3 content up to 5% WT. This quenching effect originates from the formation of effective heterojunctions between WO_3 and TiO_2, where the band alignment and energy level differences promote interfacial charge separation and migration. The suppressed PL intensity demonstrates reduced electron–hole recombination and increased availability of free carriers for surface redox reactions, thereby enhancing photocatalytic performance.[60] Notably, the 5% WT composite displayed the lowest PL intensity (Fig. 6(b)), suggesting optimal charge separation efficiency at this composition. However, further increasing the WO_3 content beyond 5% led to PL intensity recovery, likely due to excessive WO_3 coverage that prevents intimate TiO_2–WO_3 contact and weakens the heterojunction effect. This non-monotonic trend highlights the critical balance required between heterojunction formation and material loading for maximizing charge separation.

3.6. Photocatalytic activity measurement

The photocatalytic degradation performance of the catalysts was evaluated by degrading RhB solution at room temperature.

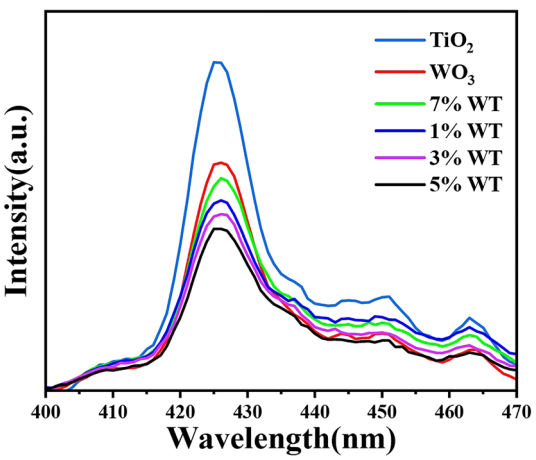

Fig. 6 Steady-state PL emission spectra of pure TiO_2, WO_3, and different WO_3@TiO_2 samples.

Fig. 7(a) and (b) presents the adsorption–degradation curves and removal efficiency of different catalysts, respectively. In the blank control group (RhB solution without a catalyst), only 4.1% degradation was observed after 30 min of irradiation, confirming the high stability of RhB. The photocatalytic degradation performance of the catalysts followed the order: 5% WT > 3% WT > 1% WT > 7% WT > TiO_2 > WO_3. Notably, all WO_3@TiO_2 composite materials exhibited significantly higher photocatalytic degradation rates than pure TiO_2 and WO_3, indicating that WO_3 and TiO_2 formed a heterojunction rather than a simple physical mixture. The 5% WT sample demonstrated the highest photocatalytic activity, achieving 99.9% RhB removal within 30 min. To quantitatively assess the photocatalytic degradation kinetics, a pseudo-first-order kinetic model was applied. As shown in Fig. 7(c) and (d), the 5% WT catalyst exhibited the highest reaction rate constant (k = 0.0128 min^{-1}), which is 29.09 times that of WO_3 (k = 0.0044 min^{-1}) and 24.15 times that of TiO_2 (k = 0.0053 min^{-1}). The remarkable enhancement in the photocatalytic activity of the WO_3@TiO_2 composites can be attributed to the following factors: (1) the broadened light absorption range facilitates the generation of more photogenerated charge carriers. (2) The heterojunction interface between TiO_2 and WO_3 promotes efficient charge separation and rapid charge transfer, thereby reducing electron–hole recombination. (3) The increased specific surface area provides more active sites for the photocatalytic reaction. The UV-Vis absorption spectra of the RhB solution during degradation over 5% WT are displayed in Fig. 7(e). The primary absorption peak of RhB appears at 554 nm, consistent with previous literature reports.[61,62] With increasing irradiation time, the overall absorbance of RhB gradually decreases, indicating the effective decomposition of its conjugated chromophore structure.[63] Moreover, the significant decline in the absorption intensity of RhB, accompanied by a gradual blue shift of the peak, suggests the occurrence of *N*-demethylation and de-ethylation reactions, confirming that RhB undergoes a stepwise degradation process. The inset in Fig. 7(e) visually illustrates the color change of the RhB solution during photocatalytic degradation. The solution color transitions from its initial rose-red to pale yellow and finally becomes colorless, indicating the complete destruction of the RhB molecular structure, consistent with previous photocatalytic degradation studies.[64]

To further evaluate the mineralization efficiency, total organic carbon (TOC) analysis was conducted. As shown in Fig. 7(f), the TOC content gradually decreases with increasing irradiation time. However, after 60 min of photocatalysis, the TOC removal efficiency only reached 68.4%, despite RhB degradation exceeding 99%. This discrepancy suggests that RhB was not fully mineralized, likely due to the generation of a significant number of low-molecular-weight by-products and intermediates, which contributed to the difference between RhB degradation and TOC removal.[65] Considering both adsorption–degradation performance and photocatalytic activity, the 5% WT sample was selected as the optimal catalyst for subsequent photocatalytic degradation experiments.

To determine the degradation threshold of the catalyst for pollutants, the degradation capability of the 5% WT sample was investigated under identical experimental conditions with RhB concentrations ranging from 5 to 70 mg L^{-1}. As shown in

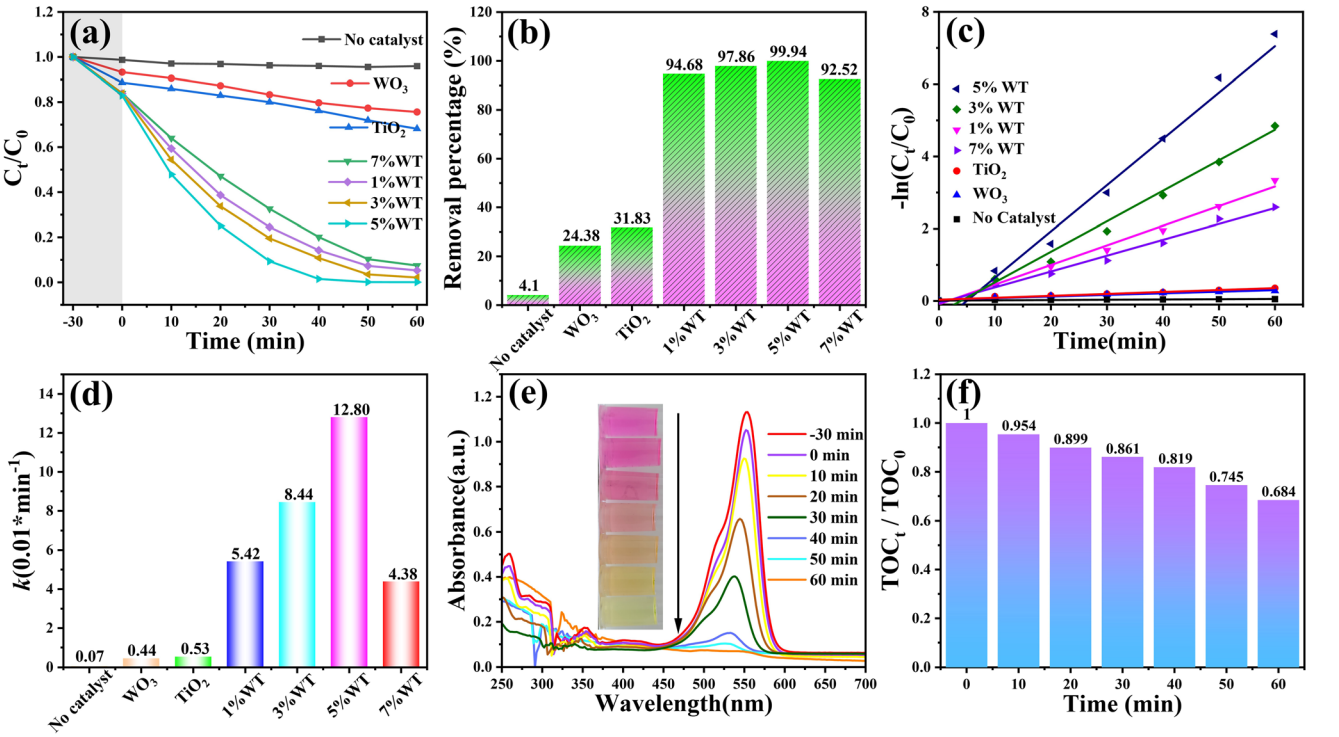

Fig. 7 (a) Adsorption–degradation curves of RhB over different catalysts; (b) removal percentage; (c) pseudo-first-order kinetic fitting; (d) degradation rate constants; (e) UV-Vis absorption spectra of RhB during degradation over 5% WT; (f) TOC variation during RhB degradation.

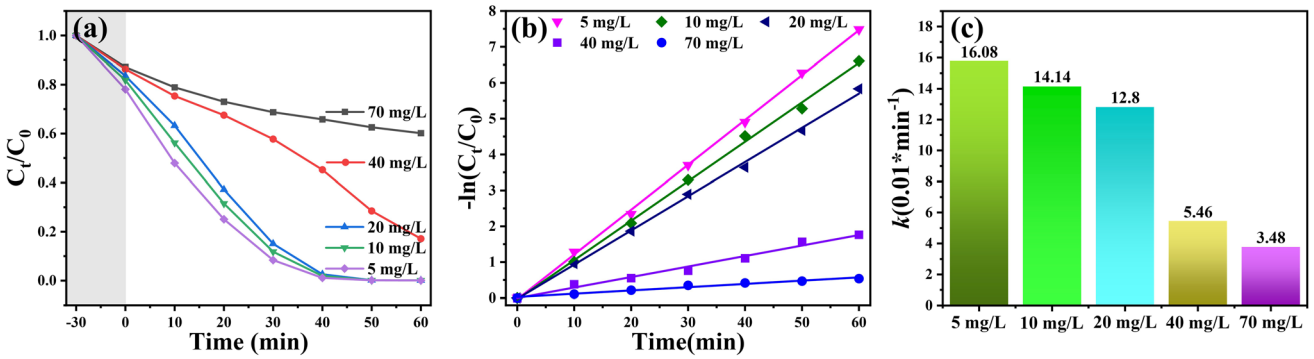

Fig. 8 Adsorption–degradation curves (a), first-order kinetic fitting (b), and degradation rate constants (c) of RhB solutions with different initial concentrations using 5% WT as the photocatalyst.

Fig. 8(a)–(c), the degradation efficiency and reaction rate of the catalyst decreased with increasing RhB concentration. Notably, when the RhB concentration increased to 40 mg L^{-1}, the degradation rate dropped significantly, with the rate constant (k = 0.0546 min^{-1}) being only 42.7% of that at 20 mg L^{-1} (k = 0.128 min^{-1}). This phenomenon can be attributed primarily to two factors. First, RhB itself is a colored dye, and at higher concentrations, it hinders the penetration of incident light, reducing the photon flux reaching the catalyst surface and subsequently decreasing the generation efficiency of photogenerated electron–hole pairs (e^-–h^+). Second, the maximum adsorption capacity of the catalyst plays a crucial role. When the pollutant concentration is excessively high, the active sites of the catalyst become fully occupied, preventing excess pollutants from participating in redox reactions, thereby leading to a decline in the degradation rate.[66]

The pH of the solution significantly influences the photocatalytic performance of the catalyst. Variations in pH can modify the surface properties of the catalyst, affect the adsorption of target compounds, and potentially alter degradation pathways. Therefore, evaluating the impact of pH on photocatalytic performance is essential. The pH of RhB aqueous solutions was adjusted within the range of 1–9 using 1 M HCl and 1 M NaOH solutions to investigate its effect on RhB degradation. As shown in Fig. 9(a), the highest removal efficiency was observed at pH = 3, where the dye was completely degraded within 50 min, whereas the removal efficiency was the lowest under strongly acidic conditions at pH = 1. When pH > 3, the degradation efficiency gradually decreased with increasing pH. Zeta potential analysis (Fig. 9(b)) revealed that the surface zeta potential of the 5% WT catalyst decreased continuously with increasing pH, with its point of zero charge (PZC) determined to be 3.1. At pH > 3.1, the catalyst surface carried a negative charge, favoring the adsorption of cations and repelling anions. Conversely, at pH < 3.1, the catalyst surface carried a positive charge, facilitating anion adsorption while repelling cations. Given that the acid dissociation constant (pK_a) of RhB is 3.7, RhB predominantly exists in its cationic form (RhB^+) at pH values below 3.7, whereas at pH values above 3.7, it exists as a zwitterionic species ($RhB^{\pm}$), a transition attributed to the deprotonation of the carboxyl group. Within the pH range of 1–3.1, electrostatic repulsion between the positively charged RhB^+ and the positively charged catalyst surface resulted in lower degradation efficiency. In the pH range of 3.1–3.7, electrostatic attraction between the negatively charged catalyst surface and RhB^+ enhanced degradation efficiency. However, when pH exceeded 3.7, the negatively charged portion of $RhB^{\pm}$ experienced electrostatic repulsion from the negatively charged catalyst surface, leading to a decline in degradation efficiency. Therefore, the optimal degradation

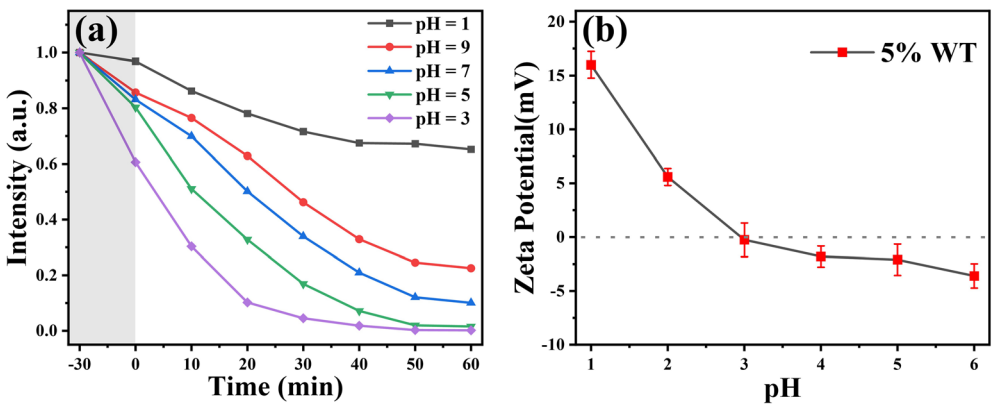

Fig. 9 (a) Adsorption–degradation curves of RhB by 5% WT under different pH conditions, (b) zeta potential of 5% WT.

conditions were observed in the pH range of 3.1–3.7, beyond which the degradation efficiency decreased.

Additionally, the degradation performance of tetracycline (TC) over the 5% WT catalyst was investigated, and the degradation process was monitored using UV-Vis spectrophotometry. As shown in Fig. 10(a), TC exhibits characteristic absorption peaks at 367 nm and 285 nm. With the progression of the photocatalytic reaction, the intensity of these peaks gradually decreases, indicating the disruption of the chromophores associated with the conjugated system,[67] a phenomenon consistent with the degradation process of RhB. Fig. 10(b) reveals that the catalyst exhibits strong adsorption capacity for TC under dark conditions, with an adsorption rate exceeding 20%. After 60 min of irradiation, the degradation efficiency of TC surpasses 90%, demonstrating the excellent photocatalytic degradation capability of 5% WT. The TC degradation process was further analyzed using a pseudo-first-order kinetic model. As depicted in Fig. 10(c), the degradation rate constant was determined to be $k = 0.0343\ \text{min}^{-1}$, with a correlation coefficient of $R^2 = 0.973$, indicating that the degradation behavior conforms well to the pseudo-first-order kinetic model. To evaluate the mineralization efficiency of organic compounds in solution, the total organic carbon (TOC) content of TC before and after photocatalytic degradation was measured. The results indicate significant mineralization of TC during photocatalysis. As shown in Fig. 10(d), after 60 min of irradiation, the TOC value of TC decreases from an initial 48.3 mg L^{-1} to 27.4 mg L^{-1}, achieving a mineralization rate of 60.3%. These findings suggest that the catalyst does not merely disrupt the chromophore structures but also facilitates the conversion of organic contaminants into inorganic products.

From the perspective of applied materials science, the recyclability of photocatalytic materials is a critical performance parameter for evaluating their practical application value. To investigate the stability of the 5% WT composite, five consecutive cyclic degradation experiments were conducted to systematically assess its photocatalytic efficiency for RhB over a reaction time of 60 min. As illustrated in Fig. 11(a), the catalyst retains over 90% of its initial degradation efficiency even after five cycles, indicating its outstanding reusability and further highlighting its feasibility for long-term practical applications. Moreover, to examine the structural stability of the photocatalyst during the reaction, the XRD patterns of the 5% WT composite before and after the cyclic degradation tests were analyzed. As shown in Fig. 11(b), the XRD patterns exhibit negligible changes after five cycles, confirming the excellent photostability of the catalyst throughout the photocatalytic process. This finding further substantiates the high stability and recyclability of the 5% WT composite, making it a promising candidate as an efficient and sustainable photocatalyst.

3.7. Photocatalytic mechanism

The migration of photogenerated charge carriers in a photocatalytic system is one of the key factors determining its overall

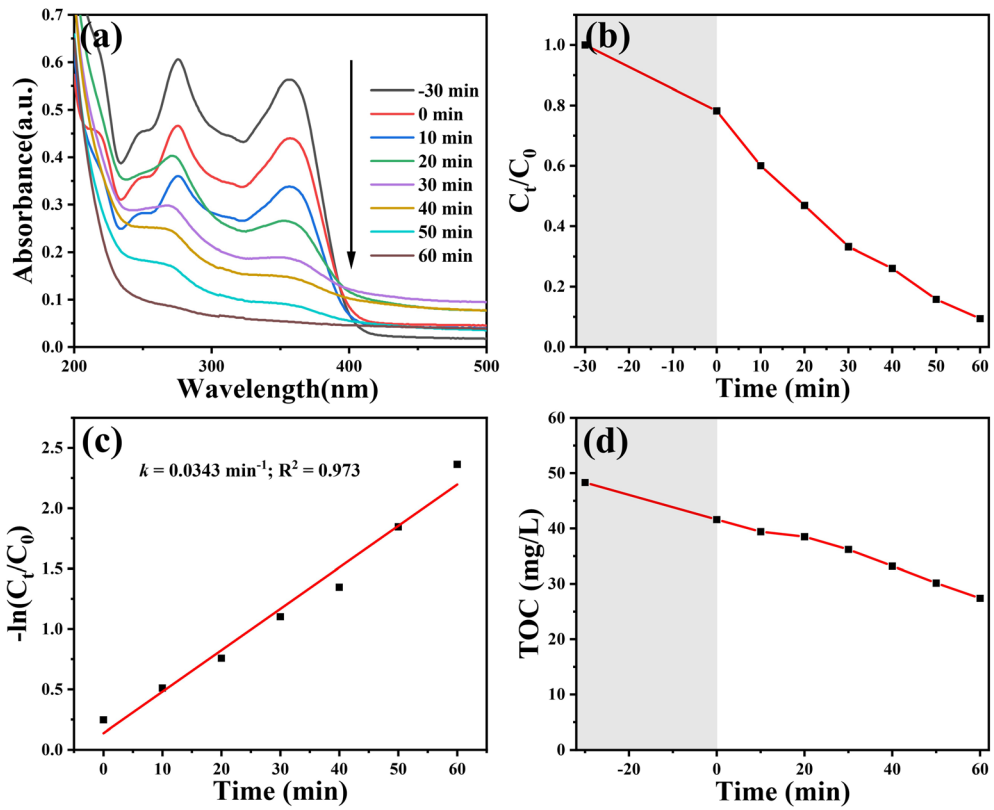

Fig. 10 (a) UV-Vis absorption spectra of tetracycline (TC) during degradation over 5% WT; (b) adsorption–degradation curves; (c) pseudo-first-order kinetic fitting curves; (d) variation in TOC values.

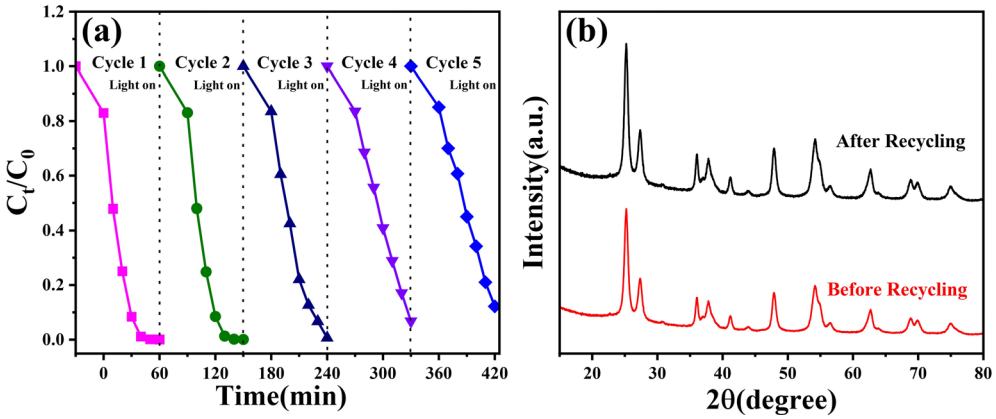

Fig. 11 (a) Photocatalytic cyclic degradation test of RhB by 5% WT; (b) XRD spectra of 5% WT before and after five cycles.

photocatalytic performance. This can be probed by transient photocurrent response measurements to evaluate charge transfer efficiency. As shown in Fig. 12(a), all samples exhibit excellent reproducibility under seven intermittent light-on and light-off cycles. In the dark, no current response is observed for any photoelectrode, confirming that the reaction is entirely driven by light. Compared to single-component materials, the 5% WT sample exhibits the highest photocurrent under illumination, indicating that the heterojunction between WO_3 and TiO_2 significantly enhances charge transfer capability. In contrast, pure WO_3 and TiO_2 photoelectrodes show much lower photocurrent responses due to severe charge carrier recombination. Notably, the relatively higher photocurrent density of the WO_3 photoelectrode compared to TiO_2 may be attributed to its hollow flower-like structure, which facilitates charge transport. Electrochemical impedance spectroscopy (EIS) was employed to characterize the surface charge transfer resistance of the materials. A smaller semicircle radius in the Nyquist plot corresponds to lower charge transfer resistance. As illustrated in Fig. 12(d), the 5% WT catalyst exhibits the smallest semicircle radius, indicating superior electrical conductivity, which is beneficial for charge carrier transport and separation of photogenerated charges. This confirms that the heterojunction between WO_3 and TiO_2 effectively reduces charge transfer resistance and promotes the separation and migration of photogenerated carriers. The valence band (VB) edge positions of

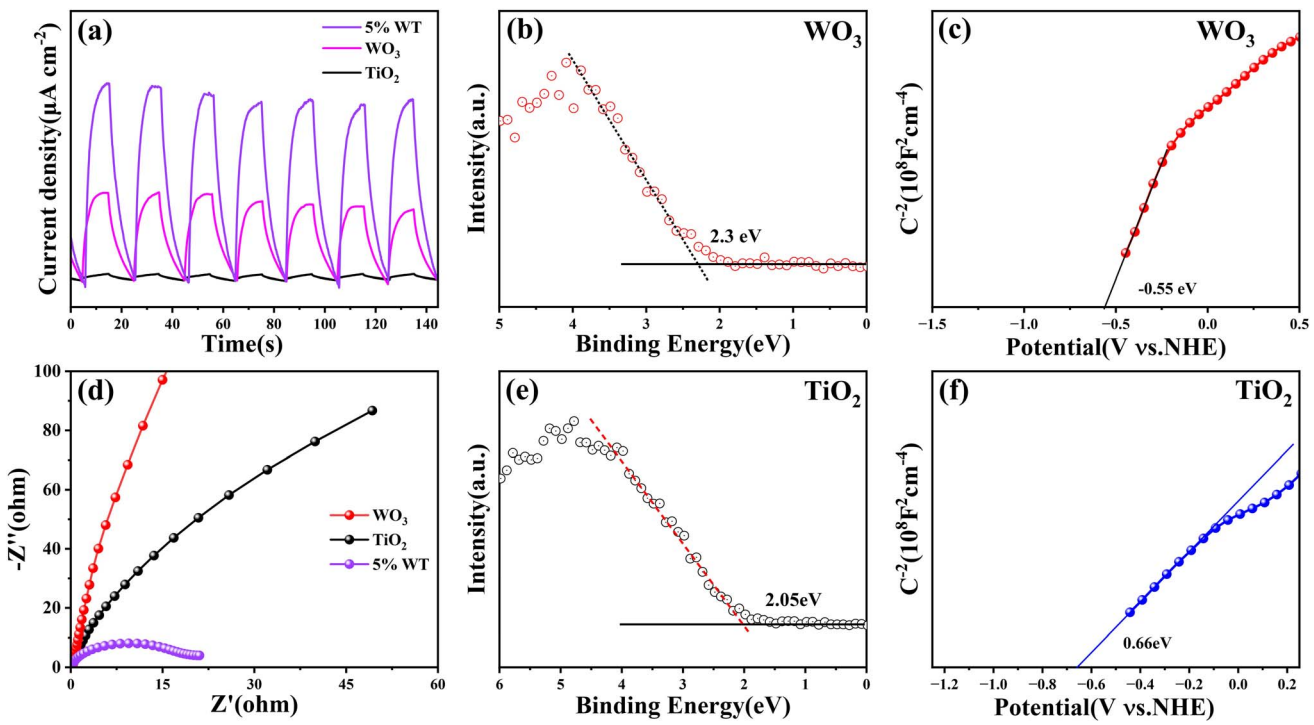

Fig. 12 (a) Transient photocurrent response of TiO_2, WO_3 and 5% WT; (b) XPS VB spectrum of WO_3; (c) Mott–Schottky plot of WO_3; (d) Nyquist plot of TiO_2, WO_3 and 5% WT; (e) XPS VB spectrum of TiO_2; (f) Mott–Schottky plot of TiO_2.

WO_3 and TiO_2 were determined by X-ray photoelectron spectroscopy (XPS) VB spectra. As shown in Fig. 12(b) and (e), the VB edge positions of WO_3 and TiO_2 are +2.3 V *vs.* NHE and +2.05 V *vs.* NHE, respectively. Combined with Tauc plots, the band gaps (E_g) of WO_3 and TiO_2 were calculated to be 2.67 eV and 3.12 eV, respectively. Based on the relationship between the conduction band (CB), valence band, and band gap ($E_{CB} = E_{VB} - E_g$), the CB edge positions of WO_3 and TiO_2 were determined to be −0.37 V and −1.07 V *vs.* NHE, respectively. To further verify the band structure of WO_3@TiO_2 composites, Mott–Schottky measurements were performed. Fig. 12(c) and (f) display the Mott–Schottky plots of WO_3 and TiO_2, with their positive slopes confirming their n-type semiconductor nature. The CB edge position was estimated from the extrapolated flat-band potential obtained from the *x*-axis intercept. The results indicate that the flat-band potentials of WO_3 and TiO_2 are −0.55 V and −0.66 V *vs.* NHE, respectively. For n-type semiconductors, the flat-band potential (which approximates the Fermi level) is typically 0.1–0.3 V above the CB edge (a midpoint value of 0.2 V was chosen in this study). Accordingly, the CB edge positions of WO_3 and TiO_2 were deduced to be −0.35 V and −0.46 V *vs.* NHE, respectively. This result is in excellent agreement with the energy band structure determined by XPS VB spectra, further validating the reliability of the band alignment.

To elucidate the potential photocatalytic mechanism of the WO_3@TiO_2 composite in pollutant degradation, radical scavenging experiments were conducted. As depicted in Fig. 13(a), in the absence of any scavengers, the WO_3@TiO_2 composite achieved a degradation efficiency of approximately 99% for RhB. However, the introduction of various scavengers significantly diminished the degradation rate. Compared to the addition of EDTA-2Na (which reduced the degradation efficiency to 48%) and IPA (which lowered it to 78%), the incorporation of BQ resulted in the most pronounced suppression, with the degradation efficiency plummeting to a mere 25%. These radical quenching experiments indicate that superoxide radicals ($^{\bullet}O_2^-$) constitute the predominant active species in the RhB degradation process. Additionally, the catalytic activity also declined upon the introduction of h^+ and $^{\bullet}OH$ scavengers, suggesting that h^+ and $^{\bullet}OH$ play significant roles in the WO_3@TiO_2-mediated photocatalytic degradation of RhB. To further substantiate the dominant contribution of $^{\bullet}O_2^-$ in the reaction, electron spin resonance (ESR) spectroscopy was employed to investigate the reaction system. As illustrated in Fig. 13(b), no signal for DMPO–$^{\bullet}O_2^-$ was detected under dark conditions. In contrast, under illumination, WO_3@TiO_2 generated a pronounced $^{\bullet}O_2^-$ signal peak, indicative of the substantial production of superoxide radicals within the system. This observation further corroborates the pivotal role of $^{\bullet}O_2^-$ in driving the photocatalytic degradation process.

Based on the aforementioned photocatalytic experiments, the most plausible photocatalytic degradation mechanism of the WO_3@TiO_2 composite is illustrated in Fig. 14. The valence band (VB) edge potential of WO_3 (+2.3 eV *vs.* NHE) surpasses that of TiO_2 (+2.05 eV *vs.* NHE), thereby establishing an internal electric field between the two semiconductors. This field facilitates the spontaneous migration of photogenerated holes from WO_3 to the VB of TiO_2. Concurrently, the conduction band (CB) edge potential of TiO_2 (−1.07 eV *vs.* NHE) is more negative than that of WO_3 (−0.37 eV *vs.* NHE), enabling the facile transfer of photogenerated electrons from the TiO_2 interface to the WO_3 interface. Moreover, the reduction potential for O_2 to form superoxide radicals ($^{\bullet}O_2^-$) (−0.33 eV *vs.* NHE) is less negative than the CB potential of WO_3 (−0.37 eV *vs.* NHE), allowing photogenerated electrons on the WO_3 CB to be readily captured

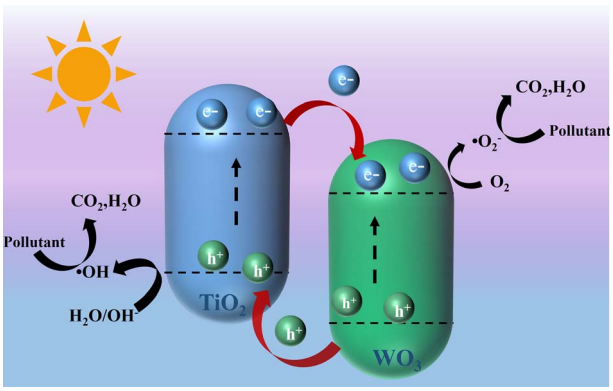

Fig. 14 Schematic diagram of WO_3@TiO_2 photocatalytic degradation of RhB.

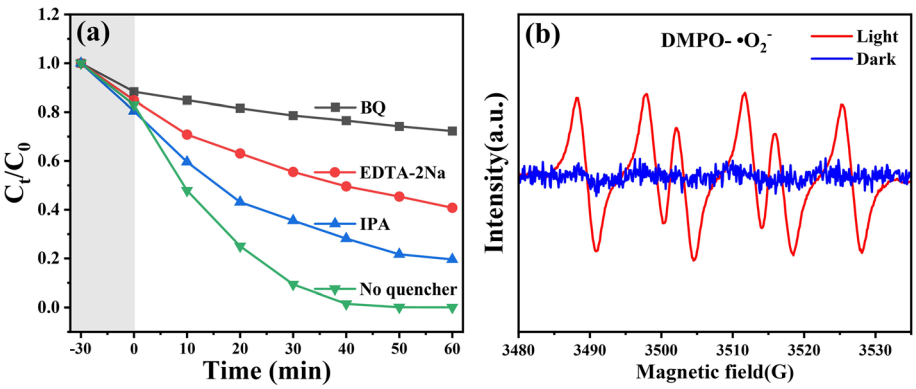

Fig. 13 (a) Degradation rate of RhB by 5% WT after adding different scavengers; (b) ESR of DMPO–$^{\bullet}O_2^-$.

by O_2, thereby generating $^{\bullet}O_2^-$. Through this electron transfer mechanism, a type-II band alignment heterojunction is established between TiO_2 and WO_3, effectively mitigating the recombination of photogenerated electrons and holes in both materials and consequently enhancing the photocatalytic performance of the composite.

4. Conclusions

In summary, this study successfully fabricated unique, uniformly sized hollow flower-like WO_3 microspheres with an internal cavity structure through a combination of solvothermal synthesis and strong acid etching. The hollow flower-like architecture not only augments the specific surface area and the availability of active sites but also enhances light absorption through its surface-dispersed nanosheet structure, thereby amplifying photocatalytic activity. TiO_2 nanoparticles were subsequently loaded onto the surface of the WO_3 microspheres *via* a sol–gel method. Experimental results revealed that the photocatalytic degradation performance of the composite initially increased with rising WO_3 content, reaching an optimum, before declining at higher concentrations. Among the synthesized materials, the 5% WT composite exhibited the most exceptional performance in photocatalytic degradation experiments, demonstrating superior photocatalytic capabilities toward both rhodamine B and tetracycline. Notably, the 5% WT composite displayed commendable degradation efficiency for RhB across a wide pH range, with optimal photocatalytic efficiency observed at pH $\approx$ 3. Through an in-depth exploration of the photocatalytic mechanism of the material, it was determined that the type-II heterojunction formed between WO_3 and TiO_2 facilitates the efficient separation of photogenerated charge carriers, thereby reducing the recombination of photogenerated charges and enhancing photocatalytic efficiency. Furthermore, through five consecutive cycling tests, the 5% WT composite demonstrated excellent reusability, a characteristic of paramount importance for cost-effectiveness and environmental sustainability in practical applications.

Data availability

Data will be made available on request.

Author contributions

The manuscript was written through contributions of all authors.

Conflicts of interest

The authors declare no competing financial interest.

Acknowledgements

W. W. and J. T. acknowledge the Natural Scientific Foundation of China (Grant No. 51603109); the State Key Project of International Cooperation Research (2023YFE0201100); the Program for Introducing Talents of Discipline to Universities ("111" plan); the High-Level Discipline Program of Shandong Province of China, and the Taishan Scholars Program (No. tsqn202408290). The authors would like to thank the Analysis and Testing Center of Qingdao University for the characterization.

References

1 A. Balakrishnan, M. M. Jacob, M. Chinthala, N. Dayanandan, M. Ponnuswamy and D.-V. N. Vo, Photocatalytic sponges for wastewater treatment, carbon dioxide reduction, and hydrogen production: a review, *Environ. Chem. Lett.*, 2024, **22**, 635–656.

2 Z. Muhammad, S. Suriati, B. Ali, L. Najeebullah, R. Nurul Ekmi and M. Nurlidia, Surface-fluorination of TiO_2 photocatalysts for remediation of water pollution: A review, *J. Cleaner Prod.*, 2021, **317**, 128354.

3 S. Bustos-Guadarrama, A. Nieto-Maldonado, L. Z. Flores-López, H. Espinoza-Gomez and G. Alonso-Nuñez, Photocatalytic degradation of azo dyes by ultra-small green synthesized silver nanoparticles, *J. Taiwan Inst. Chem. Eng.*, 2023, **142**, 104663.

4 W. Chen, W. Wang, H. Xing, W. Li, H. He, W. Li, *et al.*, Interfacial self-assembled dual-functional nanocomposite films for SERS monitoring of visible-light photocatalytic degradation of organic dye pollutants, *Surf. Interfaces*, 2023, **38**, 102808.

5 A. Khan, Z. A. Raza, H. N. Bhatti and T. Sarwar, Citrate silver nanoparticles impregnated cellulose as a photocatalytic filter in the degradation of organic dye in the aqueous media, *Int. J. Biol. Macromol.*, 2024, **261**(2), 129881.

6 W. Xiao, X. Jiang, X. Liu, W. Zhou, Z. N. Garba, I. Lawan, *et al.*, Adsorption of organic dyes from wastewater by metal-doped porous carbon materials, *J. Cleaner Prod.*, 2021, **284**, 124773.

7 J. Zeng, P. Qi, Y. Wang, Y. Liu and K. Sui, Electrostatic assembly construction of polysaccharide functionalized hybrid membrane for enhanced antimony removal, *J. Hazard. Mater.*, 2020, **410**, 124633.

8 V. Vinayagam, K. N. Palani, S. Ganesh, S. Rajesh, V. V. Akula, R. Avoodaiappan, *et al.*, Recent developments on advanced oxidation processes for degradation of pollutants from wastewater with focus on antibiotics and organic dyes, *Environ. Res.*, 2023, **240**(2), 117500.

9 L. Bai, R. Guo, Z. Chen, L. Liu, G. Dong, J. Zhang, *et al.*, Chemically fabricated $ZnO/Ag/Ag_mMo_nO_l/Zn_xMo_yO_z$ heterojunction nanophotocatalysts for abating organic dyes in wastewater, *J. Cleaner Prod.*, 2022, **363**, 132481.

10 H. Aydin, K. Sukanya, S. Jaimy, E. Paria and P. V. Nidheesh, Z-scheme photocatalysts for visible-light-driven pollutants degradation: A review on recent advancements, *Curr. Opin. Solid State Mater. Sci.*, 2021, **25**(5), 100941.

11 H. A. Maitlo, B. Anand and K.-H. Kim, TiO_2-based photocatalytic generation of hydrogen from water and wastewater, *Appl. Energy*, 2024, **361**, 122932.

12 Y. Pan, W. Liang, Z. Wang, J. Gong, Y. Wang, A. Xu, *et al.*, Facile synthesis of Pt clusters decorated TiO_2 nanoparticles for efficient photocatalytic degradation of antibiotics, *Interdiscip. Mater.*, 2024, **3**, 935–945.

13 Y. Wan, J. Li, J. Ni, C. Wang, C. Ni and H. Chen, Crystal-Facet and Microstructure Engineering in ZnO for Photocatalytic NO Oxidation, *J. Hazard. Mater.*, 2022, **435**, 129073.

14 Y. Zhang, Y. Zhang, H. Wu, Y. Wang and Q. Gu, Tandem dual-heterojunctions in $Au/ZnGa_2O_4/ZnO$ for promoted photocatalytic nonoxidative coupling of methane, *Applied Catalysis B: Environment and Energy*, 2024, **358**, 124427.

15 Y. Chen, W. Xiang, Z. Zhang, T. Ji and W. Su, Enhanced CO_2 conversion to CO using an S-scheme 2D/2D $WO_3/InVO_4$ photocatalysts, *Chem. Eng. J.*, 2025, **508**, 160993.

16 X. Zhu, Y. Zhang, Y. Wang, Y. Liu and Z. Wu, Oxygen-deficient WO_3 for stable visible-light photocatalytic degradation of acetaldehyde within a wide humidity range, *Chem. Eng. J.*, 2024, **491**, 152193.

17 Y. Yang, G. Ma, Z. An, W. Wang, X. Hu, Y. Wang, *et al.*, Preparation of recyclable g-C_3N_4/TiO_2 heterojunction/alginate hydrogel microbeads and investigation of their adsorption-photocatalytic properties, *J. Hazard. Mater. Adv.*, 2025, **18**, 100650.

18 M. A. Khan, S. Mutahir, I. Shaheen, Y. Qunhui, M. Bououdina and M. Humayun, Recent advances over the doped g-C_3N_4 in photocatalysis: A review, *Coord. Chem. Rev.*, 2024, **522**, 216227.

19 Y. Zhao, Y. Shu, X. Linghu, W. Liu, M. Di, C. Zhang, *et al.*, Modification engineering of TiO_2-based nanoheterojunction photocatalysts, *Chemosphere*, 2024, **346**, 140595.

20 N. Abd Rahman, C. E. Choong, S. Pichiah, I. W. Nah, J. R. Kim, S.-E. Oh, *et al.*, Recent advances in the TiO_2 based photoreactors for removing contaminants of emerging concern in water, *Sep. Purif. Technol.*, 2023, **304**, 122294.

21 S. Leong, A. Razmjou, K. Wang, K. Hapgood, X. Zhang and H. Wang, TiO_2 based photocatalytic membranes: A review, *J. Membr. Sci.*, 2014, **472**, 167–184.

22 S. Phromma, T. Wutikhun, P. Kasamechonchung, S. Sattayaporn, T. Eksangsri and C. Sapcharoenkun, Effects of Ag modified TiO_2 on local structure investigated by XAFS and photocatalytic activity under visible light, *Mater. Res. Bull.*, 2022, **148**, 111668.

23 W. Wang, S. Mei, H. Jiang, L. Wang, H. Tang and Q. Liu, Recent advances in TiO_2-based S-scheme heterojunction photocatalysts, *Chin. J. Catal.*, 2023, **55**, 137–158.

24 C. Xu, D. Li, X. Liu, R. Ma, N. Sakai, Y. Yang, *et al.*, Direct Z-scheme construction of g-C_3N_4 quantum dots/TiO_2 nanoflakes for efficient photocatalysis, *Chem. Eng. J.*, 2022, **430**, 132861.

25 L. Ma, G. Wang, C. Jiang, H. Bao and Q. Xu, Synthesis of core-shell TiO_2@g-C_3N_4 hollow microspheres for efficient photocatalytic degradation of rhodamine B under visible light, *Appl. Surf. Sci.*, 2018, **430**, 263–272.

26 R. Zhong, Z. Zhang, H. Yi, L. Zeng, C. Tang, L. Huang, *et al.*, Covalently bonded 2D/2D O-g-C_3N_4/TiO_2 heterojunction for enhanced visible-light photocatalytic hydrogen evolution, *Appl. Catal., B*, 2018, **237**, 1130–1138.

27 P. Chang, Y. Wang, Y. Wang and Y. Zhu, Current trends on In_2O_3 based heterojunction photocatalytic systems in photocatalytic application, *Chem. Eng. J.*, 2022, **450**(1), 137804.

28 T. Li, N. Tsubaki and Z. Jin, S-scheme heterojunction in photocatalytic hydrogen production, *J. Mater. Sci. Technol.*, 2023, **169**, 82–104.

29 M.-Z. Qin, W.-X. Fu, H. Guo, C.-G. Niu, D.-W. Huang, C. Liang, *et al.*, 2D/2D Heterojunction systems for the removal of organic pollutants: A review, *Adv. Colloid Interface Sci.*, 2021, **297**, 102540.

30 X. Wu, G. Chen, L. Li, J. Wang and G. Wang, $ZnIn_2S_4$-based S-scheme heterojunction photocatalyst, *J. Mater. Sci. Technol.*, 2023, **167**, 184–204.

31 W. Luan, Y. Yan, J. Wang, Y. Zong, R. Zhao, J. Han, *et al.*, Fabrication of In-doped CdSe/$Zn_3In_2S_6$ type II heterojunction composite for efficient photocatalytic hydrogen evolution, *Sep. Purif. Technol.*, 2025, **356**(B), 129907.

32 B. Wen, Y. Fu, J. Ma, X. Guo, Y. Liu and Z. Jin, Co-Fe Prussian blue Analogues encapsulated graphdiyne nanosheets formed type-II heterojunction for photocatalytic H_2 evolution, *Sep. Purif. Technol.*, 2025, **357**(B), 130172.

33 X. Kuang, X. Deng, Y. Ma, J. Zeng, B. Zi, Y. Zhang, *et al.*, Type II heterojunction promotes photoinduced effects of TiO_2 for enhancing photocatalytic performance, *J. Mater. Chem. C*, 2022, **10**, 6341–6347.

34 A. H. Navidpour, M. B. Ahmed and J. L. Zhou, Photocatalytic Degradation of Pharmaceutical Residues from Water and Sewage Effluent Using Different TiO_2 Nanomaterials, *Nanomaterials*, 2024, **14**(2), 135.

35 Q. Shi, Y. Zhang, D. Sun, S. Zhang, T. Tang, X. Zhang, *et al.*, Bi_2O_3-Sensitized TiO_2 Hollow Photocatalyst Drives the Efficient Removal of Tetracyclines under Visible Light, *Inorg. Chem.*, 2020, **59**(24), 18131–18140.

36 W. Wang, J. Fang, S. Shao, M. Lai and C. Lu, Compact and uniform TiO_2@g-C_3N_4 core-shell quantum heterojunction for photocatalytic degradation of tetracycline antibiotics, *Appl. Catal., B*, 2017, **217**, 57–64.

37 Y. Xu, D. Yuan, Y. Guo, S. Chen, W. Lin, Y. Long, *et al.*, Superhydrophilic and polyporous nanofibrous membrane with excellent photocatalytic activity and recyclability for wastewater remediation under visible light irradiation, *Chem. Eng. J.*, 2022, **427**, 131685.

38 U. Habiba, M. S. Islam, T. A. Siddique, A. M. Afifi and B. C. Ang, Adsorption and photocatalytic degradation of anionic dyes on Chitosan/PVA/Na–Titanate/TiO_2 composites synthesized by solution casting method, *Carbohydr. Polym.*, 2016, **149**, 317–331.

39 Y. Chen, G. Liu, L. Dong, X. Liu, M. Liu, X. Wang, *et al.*, A microwave-assisted solvothermal method to synthesize BiOCl microflowers with oxygen vacancies and their enhanced photocatalytic performance, *J. Alloys Compd.*, 2023, **930**, 167331.

40 Q. Du, Y. Lin, S. Cheng, D. Wei, Y. Wang and Y. Zhou, In situ synthesis of three-dimensional flower-like TiO_2/WO_3 heterojunction: Enhanced visible photocatalytic properties and theoretical calculations, *Ceram. Int.*, 2024, **50**(17, B), 30605–30616.

41 H. Wang, L. Jing, H. Zhang, A. Varamesh, Y. Yan, Q. Gao, *et al.*, Novel flower-like $SnIn_4S_8/WO_3$ S-scheme heterojunction photocatalysts for enhanced oxidation of 5-hydroxymethylfurfural, *J. Energy Chem.*, 2025, **105**, 373–384.

42 M. Xu, H. Nan, H. Yang, C. Xue, H. Fu, G. Yang, *et al.*, An Efficient, Multi-element $AC/TiO_2/WO_3$ Photocatalyst for the Degradation of Tetracycline Hydrochloride, *ChemistrySelect*, 2022, **7**(8), e202102883.

43 H. Wang, Q. Gong, H. Huang, T. Gao, Z. Yuan and G. Zhou, P-n heterostructured TiO_2/NiO double-shelled hollow spheres for the photocatalytic degradation of papermaking wastewater, *Mater. Res. Bull.*, 2018, **107**, 397–406.

44 R. Bao, Y. Yu, H. Chen, W. Wang, J. Xia and H. Li, Effects of Rare Earth Elements and Nitrogen Co-Doped on the Photocatalytic Performance of TiO_2, *Cryst. Res. Technol.*, 2018, **53**(2), 1700138.

45 X. Zhou, Y. Xian, Z. Li, C. Yujie, J. Luo, X. Ning, *et al.*, All-solid-state red phosphorus/RGO/WO_3 Z-scheme heterostructure for photocatalytic overall water splitting, *Sep. Purif. Technol.*, 2024, **357**(A), 130117.

46 S. Meng, W. Sun, S. Zhang, X. Zheng, X. Fu and S. Chen, Insight into the Transfer Mechanism of Photogenerated Carriers for WO_3/TiO_2 Heterojunction Photocatalysts: Is It the Transfer of Band–Band or Z-Scheme? Why?, *J. Phys. Chem. C*, 2018, **122**(46), 26326–26336.

47 H. Shi, S. Zhang, X. Zhu, Y. Liu, T. Wang, T. Jiang, *et al.*, Uniform Gold-Nanoparticle-Decorated {001}-Faceted Anatase TiO2 Nanosheets for Enhanced Solar-Light Photocatalytic Reactions, *ACS Appl. Mater. Interfaces*, 2017, **9**(42), 36907–36916.

48 X. An, Z. Shang, Y. Bai, H. Liu and J. Qu, Synergetic Photocatalytic Pure Water Splitting and Self-Supplied Oxygen Activation by 2D WO_3/TiO_2 Heterostructures, *ACS Sustain. Chem. Eng.*, 2019, **7**(24), 19902–19909.

49 J. Wang, G. Wang, B. Cheng, J. Yu and J. Fan, Sulfur-doped g-C_3N_4/TiO_2 S-scheme heterojunction photocatalyst for Congo Red photodegradation, *Chin. J. Catal.*, 2021, **42**(1), 56–68.

50 W. Gan, X. Fu, J. Jin, J. Guo, M. Zhang, R. Chen, *et al.*, Nitrogen-rich carbon nitride (C_3N_5) coupled with oxygen vacancy TiO_2 arrays for efficient photocatalytic H_2O_2 production, *J. Colloid Interface Sci.*, 2024, **653**, 1028–1039.

51 I. S. Hwang, V. Manikandan, R. P. Patil, M. A. Mahadik, W.-S. Chae, H.-S. Chung, *et al.*, Hydrogen-Treated TiO_2 Nanorods Decorated with Bimetallic Pd–Co Nanoparticles for Photocatalytic Degradation of Organic Pollutants and Bacterial Inactivation, *ACS Appl. Nano Mater.*, 2023, **6**(3), 1562–1572.

52 M. Hunsom, N. Kunthakudee, P. Ramakul, K. Serivalsatit, S. Sangkhanak, P. Wongyongnoi, *et al.*, Rapid photocatalytic gold recovery from industrial cyanide-based gold plating wastewater via TiO_2/WO_3 nanocomposites: Role of mixed hole scavengers and operating conditions, *J. Environ. Chem. Eng.*, 2023, **11**(5), 110534.

53 X. Xu, Y. Xiao, R. Zhao, Z. Yin, H. A. Butt, M. Li, *et al.*, Tailored TiO_2/WO_3 composites for enhanced electrocatalytic and photocatalytic applications, *Ceram. Int.*, 2025, **51**(10), 13586–13596.

54 T. Tatsuma, S. Saitoh, P. Ngaotrakanwiwat, Y. Ohko and A. Fujishima, Energy Storage of TiO_2—WO_3 Photocatalysis Systems in the Gas Phase, *Langmuir*, 2002, **18**(21), 7777–7779.

55 A. Ait-karra, A. Mourak, O. Zakir, A. Almaggoussi, R. Idouhli, A. Abouelfida, *et al.*, Effect of hydrothermal temperature on the structural, morphological, optical properties and photocatalytic performances of cobalt sulfide nanomaterials, *J. Alloys Compd.*, 2024, **999**, 174946.

56 R. M. Carlos and H. M.-P. Alma, Photocatalytic performance of β-Ga_2O_3 microcubes towards efficient degradation of malachite green, *Ceram. Int.*, 2021, **48**(7), 9746–9752.

57 J. Li, Y. Wang, H. Song, Y. Guo, S. Hu, H. Zheng, *et al.*, Photocatalytic hydrogen under visible light by nitrogen-doped rutile titania graphitic carbon nitride composites: an experimental and theoretical study, *Adv. Compos. Hybrid Mater.*, 2023, **6**(2), 83.

58 J. Tang, J. Wang, L. Tang, C. Feng, X. Zhu, Y. Yi, *et al.*, Preparation of floating porous g-C_3N_4 photocatalyst via a facile one-pot method for efficient photocatalytic elimination of tetracycline under visible light irradiation, *Chem. Eng. J.*, 2022, **430**, 132669.

59 Y. Li, L. Shen, E. Y. B. Pun and H. Lin, Synergistic multi-selective photocatalysis and real-time optical thermometry of $CsPbBr_3$/BiOI/TiO_2@PAN flexible nanofibers, *J. Mater. Chem. A*, 2023, **11**(45), 24861–24877.

60 L. Guo, Y. Chen, Z. Ren, X. Li, Q. Zhang, J. Wu, *et al.*, Morphology engineering of type-II heterojunction nanoarrays for improved sonophotocatalytic capability, *Ultrason. Sonochem.*, 2021, **81**, 105849.

61 X. Zhang, X. Gu, Y. Song, R. Xie, S. Zhang, J. Li, *et al.*, One-step synthesis of oxygen vacancy-rich BiOBr/TiO_2 composite: Ultrafast adsorption-photocatalytic performance and mechanism, *Chem. Eng. J.*, 2024, **495**, 153261.

62 Y. Li, D. Wang, J. Liu, L. Wang, H. Wang, S. Wang, *et al.*, γ-PGA-dependent growth of BiOBr nanosheets with exposed {010} facets for enhanced photocatalytic RhB degradation, *Appl. Surf. Sci.*, 2025, **688**, 162446.

63 Z. Lin, J. Shao, J. Zhu and D. Wang, Bi-ZFO/BMO-Vo Z-scheme heterojunction photocatalysis-PMS bidirectionally enhanced coupling system for environmental remediation, *J. Mater. Sci. Technol.*, 2025, **208**, 164–175.

64 J. H. Wang, A. E. Hassan, A. M. Elewa and A. F. M. El-Mahdy, Donor–acceptor hetero[6]radialene-based three-dimensional covalent organic frameworks for organic pollutant adsorption, photocatalytic degradation, and hydrogen production activity, *J. Mater. Chem. A*, 2024, **12**(23), 14005–14021.

65 L. Ma, M. Lu, K. Li, S. Zhang, H. Liu, Y. Huang, *et al.*, Photocatalytic degradation of octadecylamine and 4-

dodecylmorpholine over titanium based photocatalyst: Activity and mechanism insights, *Chem. Eng. J.*, 2023, **472**, 144782.

66 S. Sakhaie and F. Taghipour, UV-LED silicon carbide composite photocatalytic membrane reactor for the degradation of organic contaminants, *Chemosphere*, 2023, **328**, 138593.

67 J. Hualin, W. Qi, C. Pinghua, Z. Huitao, S. Jinwen, S. Hongying, *et al.*, Photocatalytic degradation of tetracycline by using a regenerable (Bi)BiOBr/rGO composite, *J. Cleaner Prod.*, 2022, **339**, 130771.